Optimal Gear Shift Schedule Design for Automated Vehicles: Hybrid System Based Analytical Approach

Chaozhe R. He, Wubing B. Qin, Necmiye Ozay, and Gábor Orosz

***Abstract*— In this paper, we present a systematic design framework for gear shift schedule using hybrid system theory primarily intended for automated vehicles. The longitudinal motion of the vehicle is regulated by a PI controller that determines the required axle torque. The longitudinal dynamics of the vehicle with a gear box is modeled as a hybrid system, and an optimization-based gear shift schedule design is introduced. This guarantees that the propulsion requirements are delivered while minimizing fuel consumption. The resulting dynamics is proven to be stable in the presence of constraints. We apply our framework to heavy-duty vehicle gear shift schedule design and evaluate the performance of the controller using numerical simulations.**

***Index Terms*— Automated vehicle, fuel economy, gear shift schedule design, hybrid system, stability.**

I. Introduction

NOWADAYS, ground vehicles with increased level of autonomy and connectivity are becoming available due to their potentials for improving safety, mobility, and fuel economy [1]. In particular, for the longitudinal dynamics, features, such as adaptive cruise control, are available in many cars, and advanced concepts, such as connected cruise control, are studied in academia and industry [2]–[4]. Current connected and automated vehicle development usually focuses on high-level controllers while relying on the traditional propulsion system design. However, utilizing these technologies in the propulsion system may allow significant improvements in efficiency and reliability.

Most ground vehicles are propelled by powertrains that use transmissions to match the vehicle state with the state of the engine. Transmissions enable reasonable sized engines to drive the vehicles in a wide range of speed. Ground vehicles driven on the U.S. roads are typically equipped with automatic transmission (AT) or automated manual transmission (AMT), which shifts gear in response to driver command [5]. Designing the gear shift schedule appropriately allows one to improve the fuel economy, and therefore, it is a key component of transmission design. Traditional gear shift schedules are typically designed as a static map on the plane of the driver command (throttle/pedal position) and vehicle speed.

A recent trend in a gear shift schedule design is to focus on better interpretation of the driver's intention and estimation of road environment [6]–[12]. However, including driver demand in the gear shift schedule design explicitly can make the design very challenging, and optimality may be difficult to achieve. For connected and automated vehicles, axle torque demand is explicitly assigned, and thus can be met by setting the engine torque and the gears appropriately while bypassing the need for monitoring driver demand. As shown in Fig. 1, the gear shift schedule design can be carried out based on torque demand and vehicle speed, while the design parameters have clear physical meanings and can be adjusted according to driving conditions. With a properly designed pedal-torque map, the same gear shift schedule can also be used in the human driven mode. Moreover, the automated vehicle may utilize traffic information to meet the torque demand while minimizing fuel consumption, so that the drivability and towing ability of the vehicle are not compromised. Meeting all these requirements in a reliable manner requires a rigorous mathematical approach.

The dynamics of an automated vehicle with AT/AMT can be modeled as a hybrid system, which contains dynamic variables of both discrete and continuous types [13]–[15]. Analyzing the dynamics of these systems is challenging especially when the governing equations are nonlinear [16]–[18], and this is certainly the case for automobiles and trucks. Driver as an advanced controller can handle many complicated scenarios. Integrating controllers over a powertrain designed for a human driven vehicle may require a lot of efforts on testing and tuning so as to make a safe overall system for an automated vehicle. To bypass this, we take a simplified approach that is primarily tailored for automated vehicles through the framework suggested in Fig. 1. Specifically, we propose a framework for gear shift schedule design for AT/AMT that is based on a first principle dynamic model and direct optimization. By using methods from hybrid systems, we prove the stability of the gear shift design under state and input constraints. Based on our analysis, we improve the fuel economy of a class 8 heavy-duty truck.

The remainder of this paper is organized as follows. In Section II, we describe the modeling framework that

Manuscript received January 16, 2017; revised June 16, 2017; accepted August 14, 2017. Date of publication September 27, 2017; date of current version October 9, 2018. Manuscript received in final form August 27, 2017. Recommended by Associate Editor Y.-Y. Wang. *(Corresponding author: Chaozhe R. He).*

C. R. He, W. B. Qin, and G. Orosz are with the Department of Mechanical Engineering, University of Michigan, Ann Arbor, MI 48109 USA (e-mail: hchaozhe@umich.edu; wubing@umich.edu; orosz@umich.edu).

N. Ozay is with the Department of Electrical Engineering and Computer Science, University of Michigan, Ann Arbor, MI 48109 USA (e-mail: necmiye@umich.edu).

Color versions of one or more of the figures in this paper are available online at http://ieeexplore.ieee.org.

Digital Object Identifier 10.1109/TCST.2017.2747506

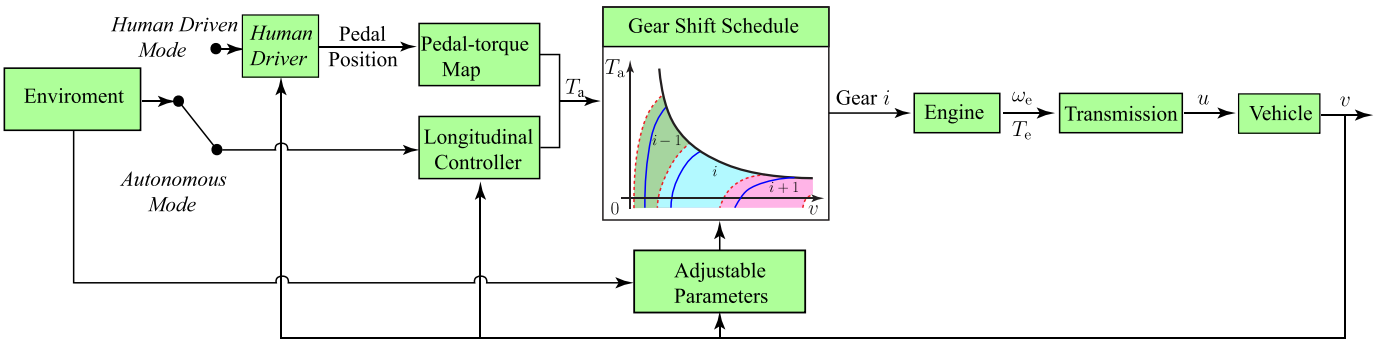

Fig. 1. Gear shift schedule implementation for automated vehicles, where T_{a} is the required axle torque, v is the speed of the vehicle, T_{e} is the engine torque, ω_{e} is the engine speed, and u is the commanded acceleration of the vehicle.

leads to a hybrid system. Then, we present the shift schedule design framework in Section III and prove that it can be used to achieve stable operating points in Section IV. In Section V, we apply the proposed design to a heavy-duty vehicle and demonstrate the effectiveness of our proposed framework under different requirements over in-production design. Finally, we conclude this paper in Section VI.

II. Vehicle Dynamics With Gear Changes

In this section, we describe the longitudinal dynamics of the vehicle with gear shift. We study forward driving only, and therefore, we develop the model for nonnegative vehicle speed. We, then, rewrite the equations using engine-based quantities to include the gear change explicitly. In order to make the problem analytically tractable, the longitudinal motion of the vehicle is modeled by differential equations, the engine fuel consumption is calculated using a static map, and the gear shifts are considered to be instantaneous.

A. Modeling Vehicle Dynamics

Here, we use the longitudinal vehicle model from [2] and [19]. Neglecting the flexibility of the suspension and the tires, Newton's second law yields

$$m_{\mathrm{eff}}\dot{v} = -mg\sin\phi - \gamma_0 mg\cos\phi - k_0(v+v_{\mathrm{w}})^2 + \frac{\eta T_{\mathrm{e}} + T_{\mathrm{b}}}{R} \tag{1}$$

where $m_{\mathrm{eff}} = m + J/R^2$ is the effective mass, containing the mass of vehicle m, the mass moment of inertia J of the rotating elements, and the wheel radius R. Also, g is the gravitational constant, ϕ is the inclination angle, γ_0 is the rolling resistance coefficient, k_0 is the air drag constant, v_{w} is the velocity of the head wind, and η is the gear ratio. Since we assume that the vehicle is traveling forward, we have $\eta > 0$. Finally, T_{e} is the engine torque, and T_{b} is the braking torque, which are the control inputs that we need to design. For simplicity, we assume that the vehicle is traveling on a flat road with no headwind, i.e., $\phi = 0$ and $v_{\mathrm{w}} = 0$. Thus, we have

$$\dot{v} = -\gamma\,\mathrm{g} - k\,v^2 + u \tag{2}$$

where

$$\gamma = \frac{m}{m_{\mathrm{eff}}}\gamma_0, \quad k = \frac{k_0}{m_{\mathrm{eff}}}, \quad u = \frac{\eta T_{\mathrm{e}} + T_{\mathrm{b}}}{m_{\mathrm{eff}} R} \tag{3}$$

and the input u has unit $[\mathrm{m/s^2}]$, so it can be considered as the commanded acceleration.

In general, the control may lead to $v < 0$. Here, we design a controller that ensures the invariance of the region $v \geq 0$. In particular, we specify the control law at $v = 0$, such that, if $u \geq \gamma\,\mathrm{g}$, $\dot{v}$ is still given by (2), while if $u < \gamma\,\mathrm{g}$, we select u, such that $\dot{v} = 0$. This is equivalent to

$$\dot{v} = -f(v) + u \tag{4}$$

where

$$f(v) = \begin{cases} \gamma\,\mathrm{g} + kv^2, & v > 0 \\ \min\{\gamma\,\mathrm{g}, u|_{v=0}\}, & v = 0. \end{cases} \tag{5}$$

In order to start the vehicle at $v = 0$, one needs $u > \gamma\,\mathrm{g}$ to obtain $\dot{v} > 0$, and otherwise, the vehicle remains stand still. On the other hand, when $v = 0$, for $u < \gamma\,\mathrm{g}$, $f(0)$ could take values, such that $\dot{v} = 0$, which makes the graph of $f(0)$ a line section instead of a single point.

For simplicity, the control input u is given by the PI controller

$$\begin{aligned} u &= K_{\mathrm{P}}\dot{w} + K_{\mathrm{I}} w \\ \dot{w} &= v_{\mathrm{r}} - v. \end{aligned} \tag{6}$$

Thus, [4]–[6] give the closed-loop dynamics

$$\begin{aligned} \dot{v} &= -f(v) + K_{\mathrm{P}}(v_{\mathrm{r}} - v) + K_{\mathrm{I}} w \\ \dot{w} &= v_{\mathrm{r}} - v \end{aligned} \tag{7}$$

that can be rewritten in terms of the variables v and u as

$$\begin{aligned} \dot{v} &= -f(v) + u \\ \dot{u} &= -K_{\mathrm{P}}(-f(v) + u - \dot{v}_{\mathrm{r}}) - K_{\mathrm{I}}(v - v_{\mathrm{r}}). \end{aligned} \tag{8}$$

When considering constant reference speed $v_{\mathrm{r}}(t) \equiv v_{\mathrm{r}}^* > 0$, system (8) possesses the equilibrium

$$\begin{aligned} v^* &= v_{\mathrm{r}}^* \\ u^* &= f\left(v_{\mathrm{r}}^*\right). \end{aligned} \tag{9}$$

Remark 1: All the analyses, in this paper, can be extended to $f(v)$ that satisfies

$$f(v) > 0, \quad \frac{\mathrm{d}f}{\mathrm{d}v} > 0, \quad \frac{\mathrm{d}^2 f}{\mathrm{d}v^2} > 0, \ \forall v > 0 \tag{10}$$

as no analysis uses explicitly the detailed form of f.

B. Introducing Gear Change

Assume that the transmission system has N gears, i.e., $\eta \in \{\eta_i | i \in \{1, 2, \ldots, N\}\}$. Then, with the ith gear applied, the angular speed of the engine and the engine torque are given by

$$\omega_{\mathrm{e}} = \frac{\eta_i}{R} v, \quad T_{\mathrm{e}} = \frac{m_{\mathrm{eff}} R}{\eta_i} u \tag{11}$$

that defines a linear transformation from the (v, u)-space to the $(\omega_{\mathrm{e}}, T_{\mathrm{e}})$-space. Henceforth, the closed-loop dynamics (8) can be rewritten as

$$\begin{aligned}
\dot{\omega}_{\mathrm{e}} &= \tfrac{\eta_i}{R} f\left(\tfrac{R}{\eta_i}\omega_{\mathrm{e}}\right) + \tfrac{\eta_i^2}{m_{\mathrm{eff}} R^2} T_{\mathrm{e}} \\
\dot{T}_{\mathrm{e}} &= -\tfrac{m_{\mathrm{eff}} R K_{\mathrm{P}}}{\eta_i}\left(-f\left(\tfrac{R}{\eta_i}\omega_{\mathrm{e}}\right) + \tfrac{\eta_i}{m_{\mathrm{eff}} R} T_{\mathrm{e}} - \dot{v}_{\mathrm{r}}\right) \\
&\quad - \frac{m_{\mathrm{eff}} R K_{\mathrm{I}}}{\eta_i}\left(\frac{R}{\eta_i}\omega_{\mathrm{e}} - v_{\mathrm{r}}\right).
\end{aligned} \tag{12}$$

With gear change, this can be written into the compact form

$$\begin{aligned}
&\begin{bmatrix} \dot{\omega}_{\mathrm{e}}(t) \\ \dot{T}_{\mathrm{e}}(t) \end{bmatrix} = F_i(\omega_{\mathrm{e}}(t), T_{\mathrm{e}}(t), v_{\mathrm{r}}(t)), \quad \text{if } [\dot{\omega}_{\mathrm{e}}(t), \dot{T}_{\mathrm{e}}(t)] \in \mathscr{X}_i \\
&\begin{bmatrix} \omega_{\mathrm{e}}(t^+) \\ T_{\mathrm{e}}(t^+) \\ i(t^+) \end{bmatrix} = S(\omega_{\mathrm{e}}(t^-), T_{\mathrm{e}}(t^-), i(t^-)), \\
&\qquad \text{if } [\omega_{\mathrm{e}}(t^-), T_{\mathrm{e}}(t^-)] \in \partial\mathscr{X}_{i(t^-)}
\end{aligned} \tag{13}$$

for $i \in \{1, \ldots, N\}$. The function F_i represents the right-hand side of (12), and it describes the continuous time dynamics for gear i when the state evolves inside the set $\mathscr{X}_i$. Moreover, S represents the gear shift schedule to be designed and describes the switches at the boundary of the set $\mathscr{X}_i$ (denoted by $\partial\mathscr{X}_i$), while t^- and t^+ denote the moment right before and right after a gear shift, respectively. In Section III, we design the gear shift schedule to achieve optimal fuel consumption, while in Section IV, we formally prove that the proposed design guarantees the stability of the overall hybrid system (13), that is, the stability of the equilibrium (9) of system (8) under gear change.

III. Gear Shift Schedule Design

In this section, we explain the gear shift design process. For simplicity, we assume that the efficiency coefficients of torque delivery at different gears are the same. As shown by the numbers in Table III, this is a very good approximation.

A. Design Process

The goal of gear shift schedule design is to select the gear that minimizes the fuel consumption while allowing the transmission to deliver the acquired torque/power. The fuel consumption can be quantified by measuring the mass flow rate of fuel $\dot{m}_{\mathrm{f}} = q(\omega_{\mathrm{e}}, T_{\mathrm{e}})$ as a function of the engine speed ω_{e} and engine torque T_{e}. To determine how efficiently the engine uses fuel while producing power $P = \omega_{\mathrm{e}} T_{\mathrm{e}}$, one can use the brake specific fuel consumption (BSFC) defined by

$$\mathrm{BSFC} = g(\omega_{\mathrm{e}}, T_{\mathrm{e}}) = \frac{\dot{m}_{\mathrm{f}}}{P} = \frac{q(\omega_{\mathrm{e}}, T_{\mathrm{e}})}{\omega_{\mathrm{e}} T_{\mathrm{e}}} \tag{14}$$

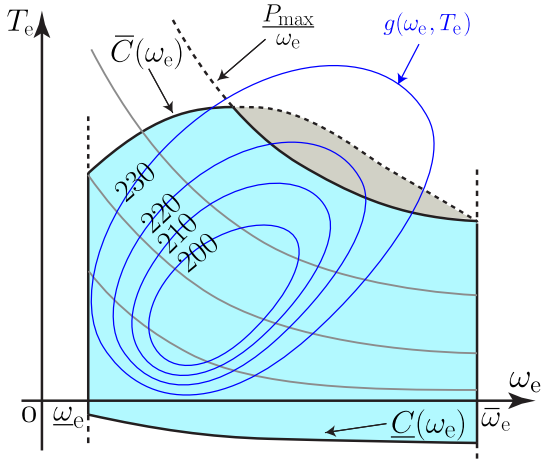

Fig. 2. Conceptual BSFC map. The blue contours correspond to the constant levels of BSFC $g(\omega_{\mathrm{e}}, T_{\mathrm{e}}) = c$, the gray curves represent the iso-power curves and the black curves represent the limitation of the engine. Since the gray region is only accessible in certain gears, the blue region is considered as the engine operating region. (Best viewed in color.)

(see [20]). Therefore, minimizing BSFC increases fuel efficiency. In practice, the function $g(\omega_{\mathrm{e}}, T_{\mathrm{e}})$ is nonlinear and does not have an analytical expression, but it may be acquired experimentally and one may use interpolation to obtain the value of g for combination of $(\omega_{\mathrm{e}}, T_{\mathrm{e}})$, where measurements are not available.

In Fig. 2, the contours of a conceptual BSFC map are plotted as blue curves, together with the maximum and minimum constraints on the engine torque and engine speed, i.e., $\underline{C}(\omega_{\mathrm{e}}) \leq T_{\mathrm{e}} \leq \overline{C}(\omega_{\mathrm{e}})$ and $\underline{\omega}_{\mathrm{e}} \leq \omega_{\mathrm{e}} \leq \overline{\omega}_{\mathrm{e}}$. Note that the gray region is only accessible in certain gears (i.e., a gear change would lead to a working point where the engine limitation is exceeded) and it is typically very small in practice. Thus, to simplify the derivation, we use the iso-power curve corresponding to $P_{\max}$ to bound the blue operating region that is given by

$$\omega_{\mathrm{e}} \in [\underline{\omega}_{\mathrm{e}}, \overline{\omega}_{\mathrm{e}}], \quad T_{\mathrm{e}} \in [\underline{C}(\omega_{\mathrm{e}}), \overline{C}(\omega_{\mathrm{e}})], \ T_{\mathrm{e}}\omega_{\mathrm{e}} \leq P_{\max}. \tag{15}$$

We assume that $g(\omega_{\mathrm{e}}, T_{\mathrm{e}})$ has a minimum in the operating region (15).

Also note that an engine can output negative torque, but the maximum absolute value of the negative torque is much smaller than that of the positive torque. As fuel consumption measurements are typically available for positive torque values only, we assume that the fuel consumption is zero along the minimum torque curve $\underline{C}(\omega_{\mathrm{e}})$ and use interpolation to obtain the fuel consumption for negative torque values. Still, for $T_{\mathrm{e}} \leq 0$, we use the strategy designed for small $T_{\mathrm{e}} > 0$ in order to avoid difficulties due to singularity of the BSFC at $T_{\mathrm{e}} = 0$ [see (14)].

We assume that the gear ratio is monotonically decreasing and no gear skipping is possible, that is

$$\begin{aligned}
&\eta_1 > \eta_2 > \cdots > \eta_N \\
&i(t^+) = \{i(t^-) - 1, i(t^-) + 1\}
\end{aligned} \tag{16}$$

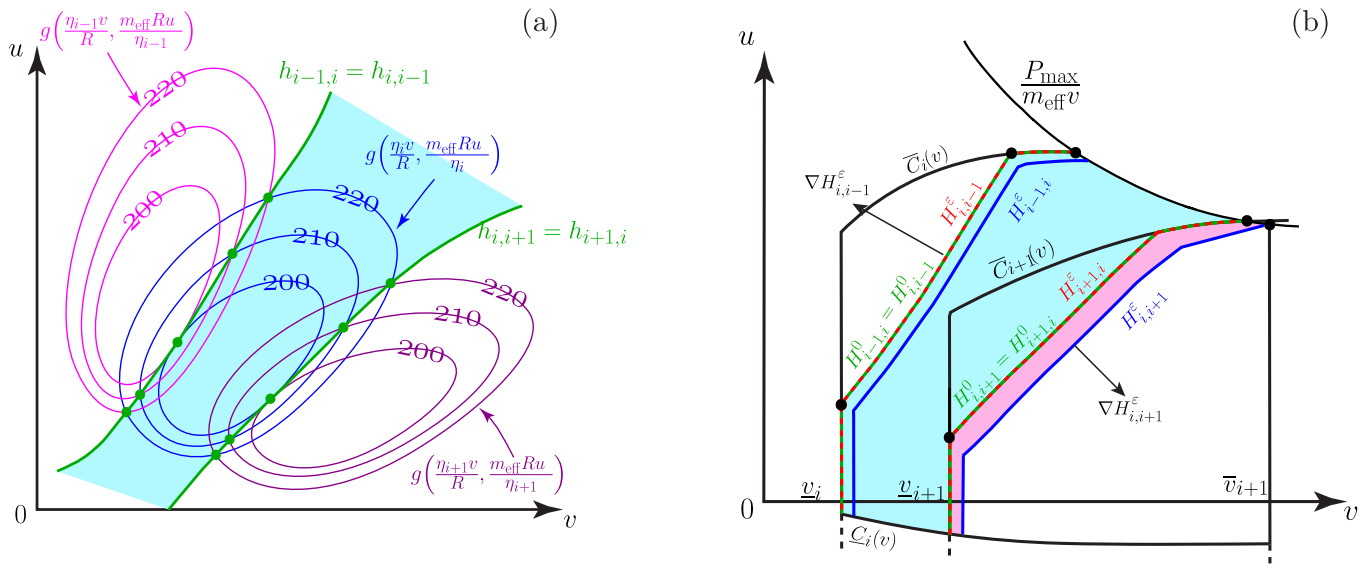

Fig. 3. Gear shift concept. (a) Magenta contours, blue contours, and purple contours represent the BSFC level sets as functions of the vehicle speed v and commanded acceleration u at the $(i-1)$st, ith, and $(i+1)$st gear, respectively. Connecting the intersections of BSFC contours results in the ideal shift curves $h_{i-1,i} = h_{i,i-1}$ and $h_{i,i+1} = h_{i+1,i}$ shown as green curves that bound the ideal working region for the ith gear highlighted as blue. (b) Capping the ideal shift curves with constraints due to engine limitations [see (15)]. The resulting constrained working region for the ith gear is bounded by the green curves $H^0_{i-1,i} = H^0_{i,i-1}$ and $H^0_{i,i+1} = H^0_{i+1,i}$, and is shaded as blue. Moving the upshift curves to $H^{\varepsilon}_{i,i+1}$ and $H^{\varepsilon}_{i-1,i}$, as shown by the blue curves, while leaving the downshift curves intact, i.e., having $H^{\varepsilon}_{i,i-1} = H^0_{i,i-1}$ and $H^{\varepsilon}_{i+1,i} = H^0_{i+1,i}$ to the right, as shown by the red dashed curves, generate overlap regions between adjacent gears. The union of the blue and the red shading is the actual working region for the ith gear denoted by $\mathscr{X}_i$. (Best viewed in color.)

for $i \in \{1, \ldots, N\}$ and $k = 1, 2, \ldots$ We also assume that shifting happens instantaneously along the iso-power curves shown as light gray curves in Fig. 2. Mathematically, such gear shift process is described as

$$m_{\text{eff}} u v = T_{\text{e},i} \omega_{\text{e},i}, \quad \frac{\omega_{\text{e},i}}{\eta_i} = \frac{\omega_{\text{e},i+1}}{\eta_{i+1}}, \quad T_{\text{e},i} \eta_i = T_{\text{e},i+1} \eta_{i+1} \tag{17}$$

for $i \in \{1, \ldots, N-1\}$.

Our gear change strategy is to choose the gear with smallest BSFC value, which is shown graphically in (v, u)-space in Fig. 3(a). The blue contours correspond to $g(\eta_i v/R, m_{\text{eff}} Ru/\eta_i) = g(\omega_{\text{e},i}, T_{\text{e},i}) = c$, the purple contours correspond to $g(\omega_{\text{e},i+1}, T_{\text{e},i+1}) = g(\eta_{i+1} v/R, m_{\text{eff}} Ru/\eta_{i+1}) = c$, while the magenta contours correspond to $g(\omega_{\text{e},i-1}, T_{\text{e},i-1}) = g(\eta_{i-1} v/R, m_{\text{eff}} Ru/\eta_{i-1}) = c$. The ideal upshift curve $h_{i,i+1}(v)$ from gear i to gear $i+1$ is determined by the solution of

$$g\left(\frac{\eta_i v}{R}, \frac{m_{\text{eff}} R h_{i,i+1}(v)}{\eta_i}\right) = g\left(\frac{\eta_{i+1} v}{R}, \frac{m_{\text{eff}} R h_{i,i+1}(v)}{\eta_{i+1}}\right) \tag{18}$$

that is visualized in Fig. 3(a) by the green curves obtained from intersections of blue and purple contours (green dots). To be able to solve (18) for the function $h_{i,i+1}(v)$, the conditions for implicit function theorem are assumed to hold. Crossing this curve to the right, i.e., shifting one gear up, shall give a smaller BSFC value. Note that this is also the ideal downshift curve from gear $i+1$ to gear i, that is, $h_{i+1,i}(v) = h_{i,i+1}(v)$. Similarly, between the ith and $(i-1)$st gear, we can construct $h_{i-1,i}(v) = h_{i,i-1}(v)$ and define the operating region for the ith gear, which is shown as the shaded blue in Fig. 3(a).

The ideal curves should be further tuned to satisfy the constraints given by the engine [see (15)], as shown in Fig. 3(b). These constraints include minimum and maximum speed constraints ($\underline{v}_i = \underline{\omega}_{\text{e}} R/\eta_i$ and $\overline{v}_i = \overline{\omega}_{\text{e}} R/\eta_i$), engine maximum torque and minimum torque ($\overline{C}_i(v)$ and $\underline{C}_i(v)$), and maximum power $P_{\max}$. The modified curves are denoted by $H^0_{i,i+1} = H^0_{i+1,i}$ and $H^0_{i-1,i} = H^0_{i,i-1}$, where the superscripts refer to the fact that the curves are given in the form $H^0_{j,k}(v, u) = 0$. These green curves bound the new ideal working region of the ith gear, indicated by blue shading in Fig. 3(b). Note that depending on the engine specification, some of the constraints above may not be part of the boundary of the working region.

The above ideal working regions will lead to ambiguity in gear selection for (v, u) pairs that sit exactly on the curve $H^0_{i,i+1} = H^0_{i+1,i}$. To avoid this, we introduce hysteresis by generating a small overlap region between the gears by splitting the curves to $H^{\varepsilon}_{i,i+1} \neq H^{\varepsilon}_{i+1,i}$. For example, between the ith and $(i+1)$st gears, we move the upshift curve to the right (that is, $H^{\varepsilon}_{i,i+1} \neq H^0_{i+1,i}$) as shown by the blue solid curve in Fig. 3(b), while keep the downshift curves at the ideal curve (that is, $H^{\varepsilon}_{i+1,i} = H^0_{i+1,i}$) as shown by the red dashed curve in Fig. 3(b). The same strategy is applied between the $(i-1)$st and the ith gears. We can now define the actual working region $\mathscr{X}_i$ for the ith gear, which is the union of the blue and the red regions in Fig. 3(b), while $\partial \mathscr{X}_i$ is given by the blue solid curves on the right and the red dashed curve on the left. Thus, the gear shift schedule (13) can be

formally written as

$$\begin{bmatrix}\omega_{\mathrm{e}}(t^+)\\ T_{\mathrm{e}}(t^+)\\ i(t^+)\end{bmatrix} = \begin{bmatrix}\omega_{\mathrm{e}}(t^-)\dfrac{\eta_{i(t^-)+1}}{\eta_{i(t^-)}}\\ T_{\mathrm{e}}(t^-)\dfrac{\eta_{i(t^-)}}{\eta_{i(t^-)+1}}\\ i(t^-)+1\end{bmatrix}$$
$$\text{if } H^{\varepsilon}_{i,i+1}\left(\omega_{\mathrm{e}}(t^-)\frac{R}{\eta_{i(t^-)}}, T_{\mathrm{e}}(t^-)\frac{\eta_{i(t^-)}}{m_{\mathrm{eff}}R}\right)=0,$$
$$\nabla H^{\varepsilon}_{i,i+1}|_{t=t^-}\cdot\begin{bmatrix}\dot{\omega}_{\mathrm{e}}(t^-)\dfrac{R}{\eta_{i(t^-)}}\\ \dot{T}_{\mathrm{e}}(t^-)\dfrac{\eta_{i(t^-)}}{m_{\mathrm{eff}}R}\end{bmatrix}>0 \qquad (19)$$

and

$$\begin{bmatrix}\omega_{\mathrm{e}}(t^+)\\ T_{\mathrm{e}}(t^+)\\ i(t^+)\end{bmatrix} = \begin{bmatrix}\omega_{\mathrm{e}}(t^-)\dfrac{\eta_{i(t^-)-1}}{\eta_{i(t^-)}}\\ T_{\mathrm{e}}(t^-)\dfrac{\eta_{i(t^-)}}{\eta_{i(t^-)-1}}\\ i(t^-)-1\end{bmatrix}$$
$$\text{if } H^{\varepsilon}_{i,i-1}\left(\omega_{\mathrm{e}}(t^-)\frac{R}{\eta_{i(t^-)}}, T_{\mathrm{e}}(t^-)\frac{\eta_{i(t^-)}}{m_{\mathrm{eff}}R}\right)=0,$$
$$\nabla H^{\varepsilon}_{i,i-1}|_{t=t^-}\cdot\begin{bmatrix}\dot{\omega}_{\mathrm{e}}(t^-)\dfrac{R}{\eta_{i(t^-)}}\\ \dot{T}_{\mathrm{e}}(t^-)\dfrac{\eta_{i(t^-)}}{m_{\mathrm{eff}}R}\end{bmatrix}>0 \qquad (20)$$

where ∇ is the gradient operator for multivariable functions [see the vectors in Fig. 3(b)] [see (17) and (18)].

In Section IV, we will show that having overlap regions between gears is crucial for the stability of system (13). The size of the overlap region will affect the performance of the gear shift schedule as will be demonstrated through a case study on a heavy-duty vehicle in Section V.

IV. Stability With Gear Changes

In this section, we prove that the hybrid system (13) is stable in the sense of Lyapunov with the proposed gear shift schedule (19) and (20). Before stating the main results of the section, we present some useful definitions, all of which are visualized graphically in Fig. 4.

Definition 1: A partition of a compact set $\mathscr{X}\subseteq\mathbb{R}^2$ is a collection of subsets $\{P_i\}_{i=1}^k$, $P_i\subseteq\mathscr{X}$, $P_i\neq\emptyset$, such that $\bigcup_{i=1}^k P_i=\mathscr{X}$ and $P_i\bigcap P_j=\emptyset, \forall i\neq j$.

As shown in Fig. 4(a), the partition means that the P_i-s covers the set $\mathscr{X}$ and that there is no intersection between the P_i-s.

Definition 2: Given a partition $\{P_i^{\mathrm{N}}\}_{i=1}^k$ of a compact set $\mathscr{X}\subseteq\mathbb{R}^2$, let $N_i=\{j\in\mathbb{N}^+\mid\partial P_i^{\mathrm{N}}\cap\partial P_j^{\mathrm{N}}\neq\emptyset, i\neq j\}$. Then, $\{P_i^{\mathrm{N}}\}_{i=1}^k$ is called a two-neighbor partition if $|N_i|\leq 2$.

Here, $|S|$ denotes the number of element of the set S and ∂S denotes the boundary of the set S. The superscript "N" stands for neighbor. The definition means that the P_i^{N}-s covers the set $\mathscr{X}$ and that each P_i^{N} has at most two neighbors [see Fig. 4(b)].

Definition 3: Given a partition $\{P_i\}_{i=1}^k$, an ε-partition of a compact set $\mathscr{X}\in\mathbb{R}^2$ is a collection of subsets $\{P_i^{\varepsilon}\}_{i=1}^k$, $P_i^{\varepsilon}\subseteq\mathscr{X}$, $P_i^{\varepsilon}\neq\emptyset$, such that $\bigcup_{i=1}^k P_i^{\varepsilon}=\mathscr{X}$ and $P_i^{\varepsilon}\backslash P_j^{\varepsilon}\neq\emptyset, \forall i\neq j$, where $\varepsilon=\inf\{\rho>0|P_i^{\varepsilon}\subseteq(P_i\bigoplus B_\rho)\cap\mathscr{X}, \forall i\}$.

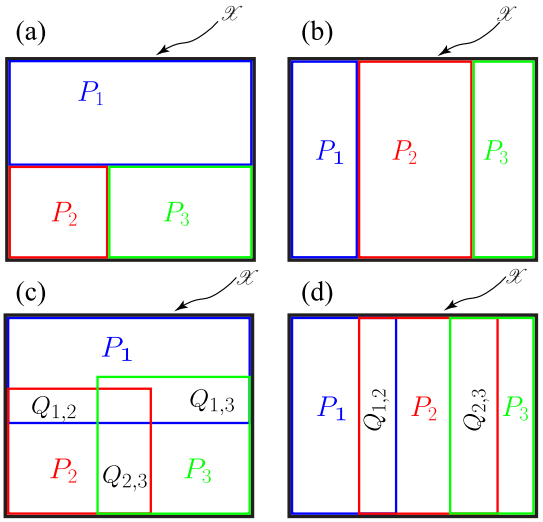

Fig. 4. Visualization of definitions. (a) Partition. (b) Two-neighbor partition. (c) ε-partition. (d) Two-neighbor ε-partition.

Here, B_ρ denotes a ball with radius ρ around the origin and $\bigoplus$ denotes the Minkowski sum defined by $A\bigoplus B=\{z=x+y|x\in A, y\in B\}$. This definition means that the P_i^{ε}-s covers the set $\mathscr{X}$ and that each P_i^{ε} overlaps with its neighbors, while ε is the smallest radius for the ball that allows us to cover the overlap regions [see Fig. 4(c)]. It is clear that as $\varepsilon\to 0$, an ε-partition $\{P_i^{\varepsilon}\}_{i=1}^k$ converges to a partition $\{P_i\}_{i=1}^k$.

Definition 4: A two-neighbor ε-partition of a compact set $\mathscr{X}$ is an ε-partition $\{P_i^{\mathrm{N}\varepsilon}\}_{i=1}^k$ of that set, such that $|N_i|\leq 2, \forall i$ and $Q_{i,j}^{\mathrm{N}\varepsilon}\bigcap Q_{i,l}^{\mathrm{N}\varepsilon}=\emptyset, \forall j,l\in N_i$ where $N_i=\{j\in\mathbb{N}^+P_i^{\mathrm{N}\varepsilon}\bigcap P_j^{\mathrm{N}\varepsilon}\neq\emptyset, i\neq j\}$ and $Q_{i,j}^{\mathrm{N}\varepsilon}=P_i^{\mathrm{N}\varepsilon}\bigcap P_j^{\mathrm{N}\varepsilon}$.

This definition means that the $P_i^{\mathrm{N}\varepsilon}$-s covers the set $\mathscr{X}$ and each $P_i^{\mathrm{N}\varepsilon}$ overlaps with its neighbors, but there will be at most two neighbors for each $P_i^{\mathrm{N}\varepsilon}$ [see Fig. 4(d)].

Lemma 1: Given a two-neighbor ε-partition of a set $\mathscr{X}$, $\{P_i^{\mathrm{N}\varepsilon}\backslash(\bigcup_{j\in N_i}Q_{i,j}^{\mathrm{N}\varepsilon})\}_{i=1}^k\bigcup\{\bigcup_{j\in N_i}Q_{i,j}^{\mathrm{N}\varepsilon}\}_{i=1}^k$ gives a partition of the set $\mathscr{X}$.

Proof: This is trivial since there is no intersection between any two intersections of any two of the partition elements $Q_{i,j}^{\mathrm{N}\varepsilon}=P_i^{\mathrm{N}\varepsilon}\bigcap P_j^{\mathrm{N}\varepsilon}$. □

Lemma 2: A full-rank affine transformation preserves partition (or ε-partition or two-neighbor partition or two-neighbor ε-partition) of a set $\mathscr{X}\subseteq\mathbb{R}^2$.

Proof: We prove this by contradiction. Suppose that the image of a partition is not a partition any more. It could be that $\bigcup_{i=1}^k P_i\neq\mathscr{X}$ or $\exists i\neq j$, $P_i\bigcap P_j\neq\emptyset$. Both cases imply that $\exists Q\in\mathrm{Im}(\mathscr{X})$, $Q\neq\emptyset$, such that $\mathrm{Pre}(Q)=\emptyset$, that is, the affine transformation maps a point to a nonempty set, which cannot be true for a full-rank affine transformation. □

Using Lemma 2, we can conclude that if the shift schedule (19) and (20) gives a two-neighbor ε-partition, it maps all the equilibria of the system (8) that are not located in an overlap region to a unique equilibrium of the switched system (13). If an equilibrium of (8) is located in the overlap

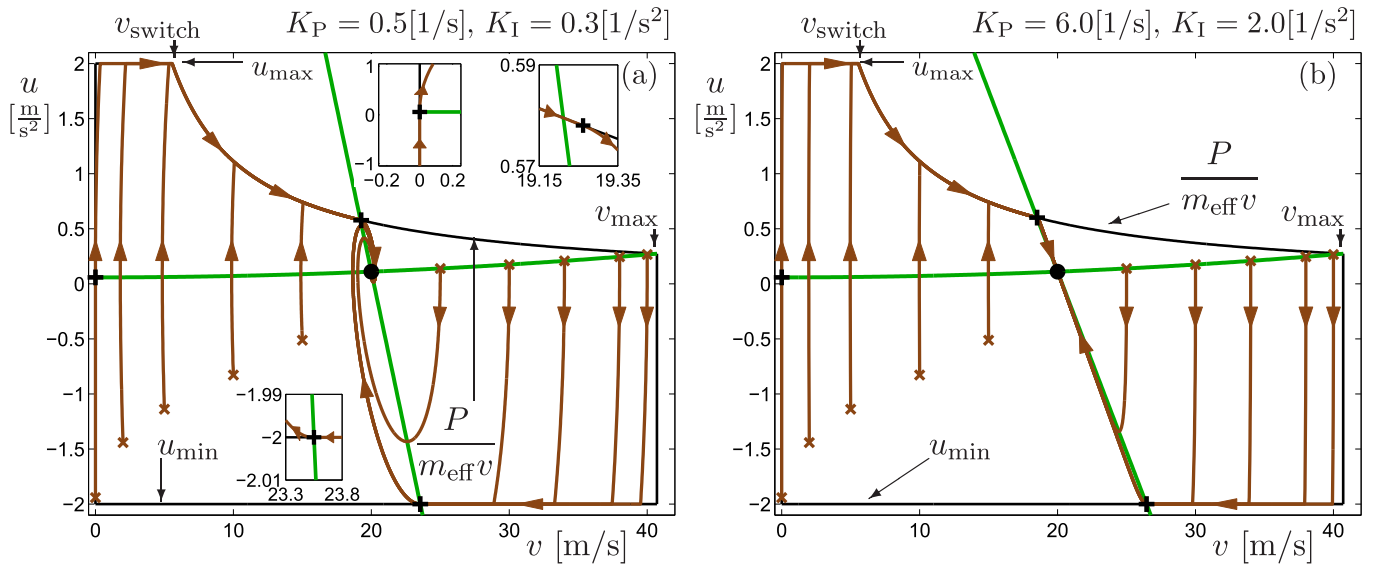

Fig. 5. Phase plane dynamics of system (8) with constraints (26) for different control parameters as indicated. Trajectories starting from different initial points are marked as brown curves. The green curves denote the nullclines $u = f(v)$, and $u = (K_{\text{I}}/K_{\text{P}})(v^* - v) + f(v)$ and they intersect at the equilibrium denoted by the black dot. The black solid pluses denote the exit points of trajectories along the boundary arcs. (Best viewed in color.)

region, the shift schedule (19) and (20) will not map it to a unique equilibrium of (13). We will deal with this issue in Theorem 1.

Next, we define the working region of (8) on the (v, u)-plane. In particular, the power limit of the engine results in

$$u \leq \frac{P_{\max}}{m_{\text{eff}} v}. \tag{21}$$

Besides this, we also impose the maximum and minimum constraints

$$u_{\min} \leq u \leq u_{\max} \tag{22}$$

where $u_{\min}$ comes from braking torque limit, and it can only be applied when $v > 0$, while $u_{\max}$ is an upper bound due to the torque limitation of the engine (e.g., $\overline{C}(\omega_{\text{e}})$), and other physical limits at low vehicle speed. The speed where (21) starts to become active and (22) starts to become inactive is given by

$$v_{\text{switch}} = \frac{P_{\max}}{m_{\text{eff}} u_{\max}}. \tag{23}$$

Note that due to the relation between w and u given by (6), (21) and (22) impose constraints on w as well. This saturation, in fact, may lead to an antiwindup mechanism that improves the performance of the PI controller [21]. Recall that according to (5), $u_{\max} > \gamma \text{g}$ is needed to start a stationary vehicle. Finally, we restrict ourselves to the speed range

$$0 \leq v \leq v_{\max} \tag{24}$$

where $v_{\max}$ is chosen to be the maximum steady-state speed given by

$$P_{\max} - m_{\text{eff}} f(v_{\max}) v_{\max} = 0. \tag{25}$$

Since f is monotonically increasing for positive speed, $v_{\max}$ is unique.

Therefore, the constrained working region is given by

$$\left\{(v, u) | v \in [0, v_{\max}], u \in \left[u_{\min}, \min\left(u_{\max}, \frac{P_{\max}}{m_{\text{eff}} v}\right)\right]\right\} \tag{26}$$

that is enclosed by the black curves in Fig. 5. Lemma 3 states the stability conditions for an equilibrium of (8) within this domain.

Lemma 3: If condition (10) holds, by choosing the feedback gains as

$$K_{\text{P}} > \frac{P_{\max}}{m_{\text{eff}} v_{\text{switch}}^2}, \quad K_{\text{I}} > K_{\text{P}} f'(v_{\max}) \tag{27}$$

the equilibrium (9) of system (8) is asymptotically stable and (26) is the region of attraction.

The details of the proof are given in Appendix A, where we propose a Lyapunov function and first show asymptotic stability of the equilibrium without constraints. Then, we show that the trajectories join and leave the boundaries of (26) at particular points [see the inlets in Fig. 5(a)] and that the value of the Lyapunov function decreases while traveling along the boundaries. We remark that the conditions on K_{P} and K_{I} in Lemma 3 are easy to satisfy, as $f'(v_{\max}) > 0$ is usually small.

In Fig. 5, we show trajectories as brown curves starting from multiple initial conditions (marked by brown crosses), for reference speed $v^* = 20[\text{m/s}]$, for two different sets of control parameters as indicated earlier. The conditions in Lemma 3 are satisfied in both cases. Indeed, all trajectories in Fig. 5 converge to the equilibrium denoted by black dots. In Fig. 5(a), the equilibrium appears as a focus, while in Fig. 5(b), it appears as a node. The green curves denote the nullclines $u = f(v)$ and $u = (K_{\text{I}}/K_{\text{P}})(v^* - v) + f(v)$ [see (8)] that intersect at the equilibrium. The nullclines are utilized in the proof in Appendix A. The black solid pluses denote the points along the boundary arcs where the

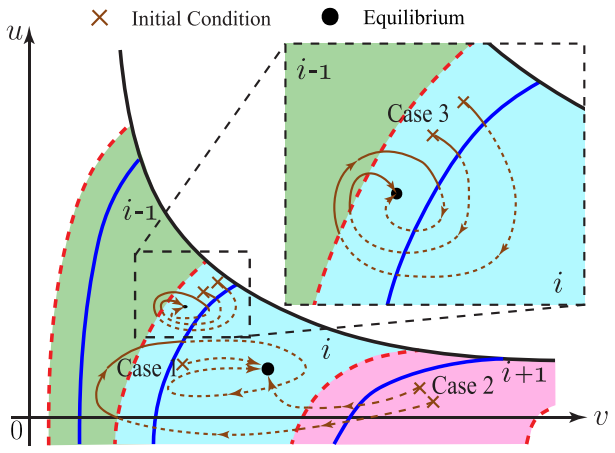

Fig. 6. Sketch of the proof of Theorem 1. Trajectories associated with different cases, with the zoomed-in view of the part of the figures. In cases 1 and 2, the equilibrium is in the nonoverlap region and the trajectory evolves either without gear change (case 1) or with finitely many gear changes (case 2). In case 3, the equilibrium is in the overlap region, and the gear at the equilibrium depends on the initial states. (Best viewed in color.)

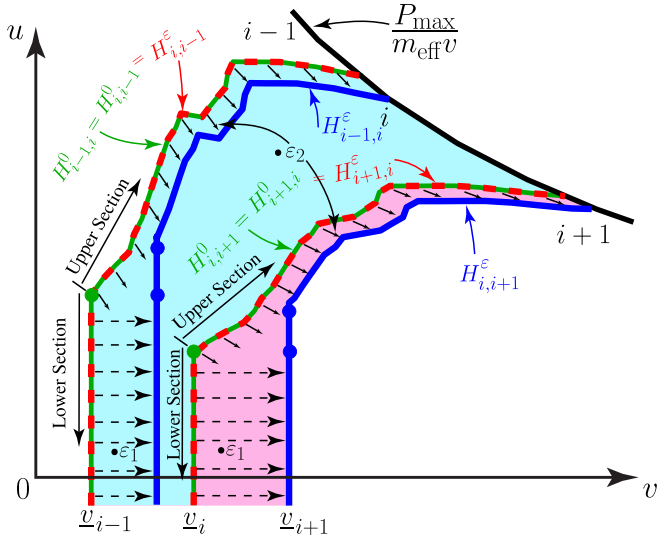

Fig. 7. Procedure of generating the two-neighbor ε-partition gear shift schedule from the ideal shift curves (green). Through the indicated shifting using ε_1 and ε_2, the actual upshift (blue) and downshift (red dashed) curves are obtained. (Best viewed in color.)

trajectories leave the arcs as highlighted by the inlets. These can be calculated analytically [see (36) in Appendix A].

Before presenting the main theorem, we require one more assumption that should be satisfied when designing the shift schedule.

Assumption 1: The gear shift schedule (19) and (20) gives a two-neighbor ε-partition in the (v, u)-space. If $\varepsilon = 0$, the gear shift schedule gives two-neighbor partitions in the (v, u)-space.

In practice, the BSFC map is usually close to a quadratic function with one minimum point, and it can be checked that for a quadratic BSFC function, Assumption 1 holds. As will be shown in the following, this assumption is essential to prove the stability of a gear switch schedule, so one shall generate a two-neighbor ε-partition in the (v, u)-plane even when the BSFC is more complicated. Based on all definitions, lemmas, and assumptions, we are now ready to present the main theorem.

Theorem 1: If Assumption 1 and Lemmas 1–3 hold, the trajectories will approach the equilibrium while having finitely many gear changes.

The details of the proof are given in Appendix B. The idea behind the proof is to categorize all different cases and show stability of the system (13), respectively. All the three different possibilities are shown in Fig. 6, where initial conditions are denoted by brown crosses, the equilibrium is denoted by black dot, and different line styles of the trajectories indicate different gears. We emphasize again that the stability of system (13) requires implicitly the fact that the gear shift schedule (19) and (20) gives a two-neighbor ε-partition in the (v, u)-space.

We remark that stability of system (13) with certain gear shift schedule does not require specific structure of the controller. The proof of Theorem 1 relies only on the fact that the equilibrium of the controlled system in (v, u)-space is stable. Therefore, the gear shift schedule design may be generalized to more general and nonlinear controllers, such as those presented in [2] and [22].

V. Application of the Gear Shift Schedule Design for a Heavy-Duty Vehicle

In this section, we apply the proposed method to the gear shift schedule design of a class 8 truck. In particular, we consider a Prostar truck manufactured by Navistar that is equipped with a MaxxForce 13 liter diesel engine and a ten speed AMT. The parameters for the vehicle are given in Table III in Appendix C. The gear ratios η_i in (16) are given by the corresponding value in Table III times the final drive ratio. Similar to the gear ratio, the efficiency is calculated by the corresponding number in Table III times the efficiency of the final drive. During simulations, the mild difference in efficiency of torque delivery at different gears is also taken into account. We also set $P_{\max} = 330$ [kW], $u_{\max} = 2[\text{m/s}^2]$, and $u_{\min} = -2[\text{m/s}^2]$, yielding $v_{\max} = 40.70[\text{m/s}]$.

Using the proposed gear shift schedule design, the ideal shift curves $H^0_{i,i+1} = H^0_{i+1,i}$ and $H^0_{i,i-1} = H^0_{i-1,i}$ are shown as green solid curves in Fig. 7. Note that each $H^0_{i,i+1}$ consists of two sections. The vertical line at the bottom up to blue dot is resulted from the low engine speed limit, i.e., $\underline{v}_i = \underline{\omega}_e \eta_i / R$. We refer to this section as the lower section. The rest of the curve $H^0_{i,i+1}$ is called the upper section. To generate a two-neighbor ε-partition in the (v, u)-space, we shift the ideal curve $H^0_{i,i+1}$ to the right in order to get the upshift curve $H^\varepsilon_{i,i+1}$ while keeping downshift curve as $H^\varepsilon_{i+1,i} = H^0_{i+1,i}$. The curve $H^\varepsilon_{i,i+1}$ is obtained in three steps. First, the lower section of $H^0_{i,i+1}$ is shifted to the right with ratio ε_1, that is, from $H^0_{i,i+1}$ to $H^0_{i,i+1} + \varepsilon_1 (H^0_{i+1,i+2} - H^0_{i,i+1})$, as shown by the black dashed arrows in Fig. 7. Second, the upper section of the new $H^0_{i,i+1}(v, u)$ is shifted along iso-power curves, that is from $H^0_{i,i+1}(v, u) = 0$ to $H^0_{i,i+1}((1+\varepsilon_2)v, u/(1+\varepsilon_2)) = 0$, as shown by the black solid arrows in Fig. 7. Finally, the upshift curve $H^\varepsilon_{i,i+1}$ is generated by extending the lower section toward

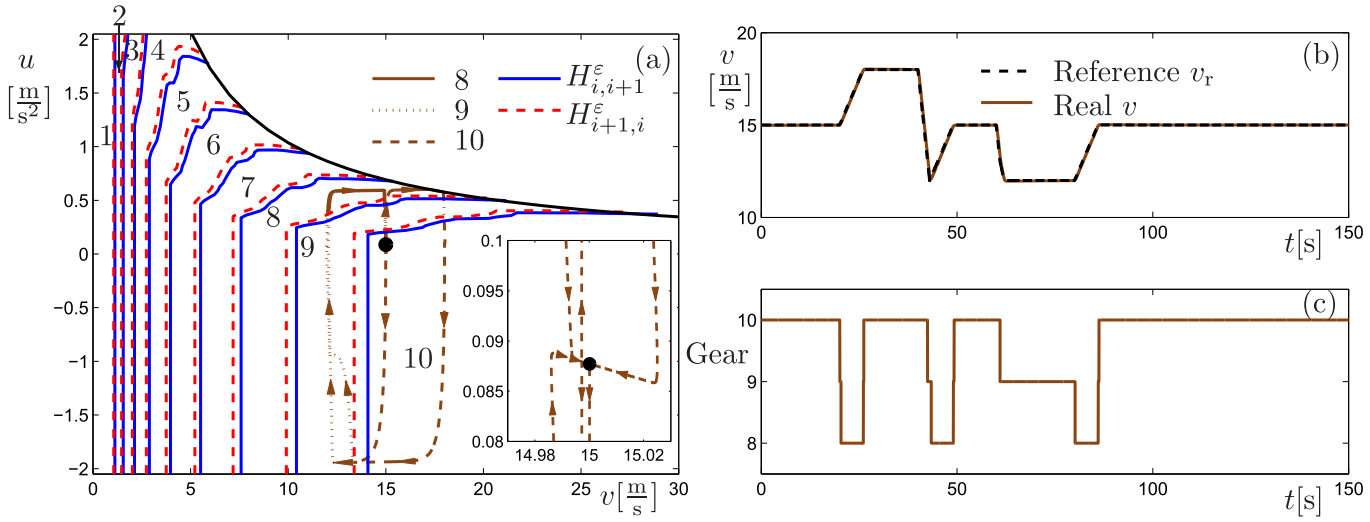

Fig. 8. Performance of the system (13) with the gear shift schedule [see (19) and (20)]. (a) Trajectory in the (v, u)-space, with the corresponding gear indicated by the line styles. (b) Time profiles of the reference speed v_r and the vehicle speed v. (c) Time profile of the gear. (Best viewed in color.)

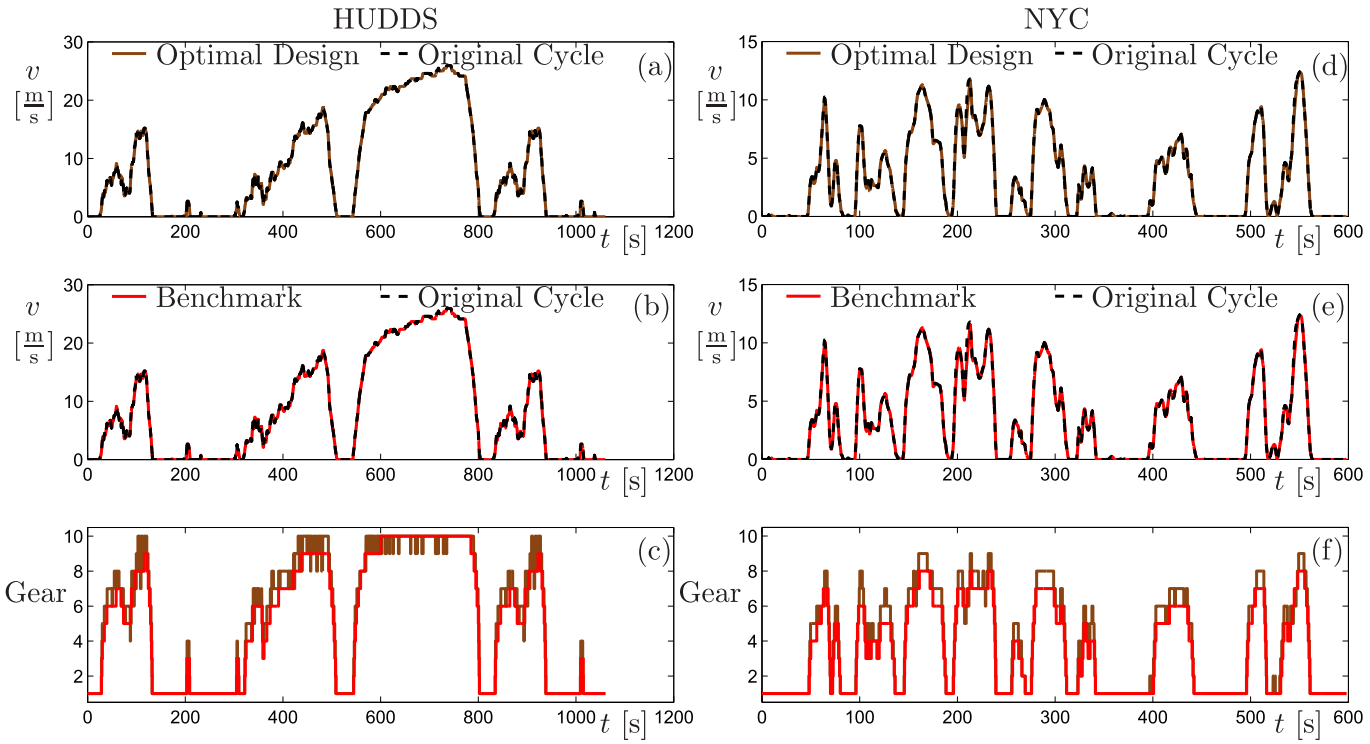

Fig. 9. Performance of the system (13) with proposed gear shift schedule while following different driving cycles. The top (a) and (d) and middle (b) and (e) rows show the speed profiles of both optimal design (brown) and in-production benchmark design (red) while following the driving cycle (dashed black). The bottom (c) and (f) row shows the corresponding gear profiles. (Best viewed in color.)

the upper section as shown by the blue curve in Fig. 7. The downshift curves are shown as red dashed curves, and they coincide with the ideal green curves.

All upshift and downshift curves are shown in the (v, u)-space in Fig. 8(a) when choosing $\varepsilon_1 = 0.15$ and $\varepsilon_2 = 0.05$. Indeed, a two-neighbor ε-partition in (v, u)-space is generated, so Assumption 1 holds, and thus, the stability of (13) is guaranteed by Theorem 1. We remark that larger ε-s leads to better drivability in traditional sense [7], as they make the vehicle stay at a lower gear compared with the ideal design, making the maximum available power larger at a given speed. On the other hand, increasing ε-s pushes the design away from the ideal curves and thus lowers the fuel economy. Thus, the ε-s can be used for tuning between fuel economy and drivability.

Numerical simulations are carried out to show the effectiveness of the proposed design. The feedback gains in (8) are set to $K_I = 0.5[1/s^2]$ and $K_P = 6[1/s]$. As the condition of Lemma 3 holds, stability of the equilibrium is guaranteed. The simulation uses a time step of 0.01 [s], and the gear shift decision made at each time step is applied in the next step. In Fig. 8(b), we first show the case where controller (6)

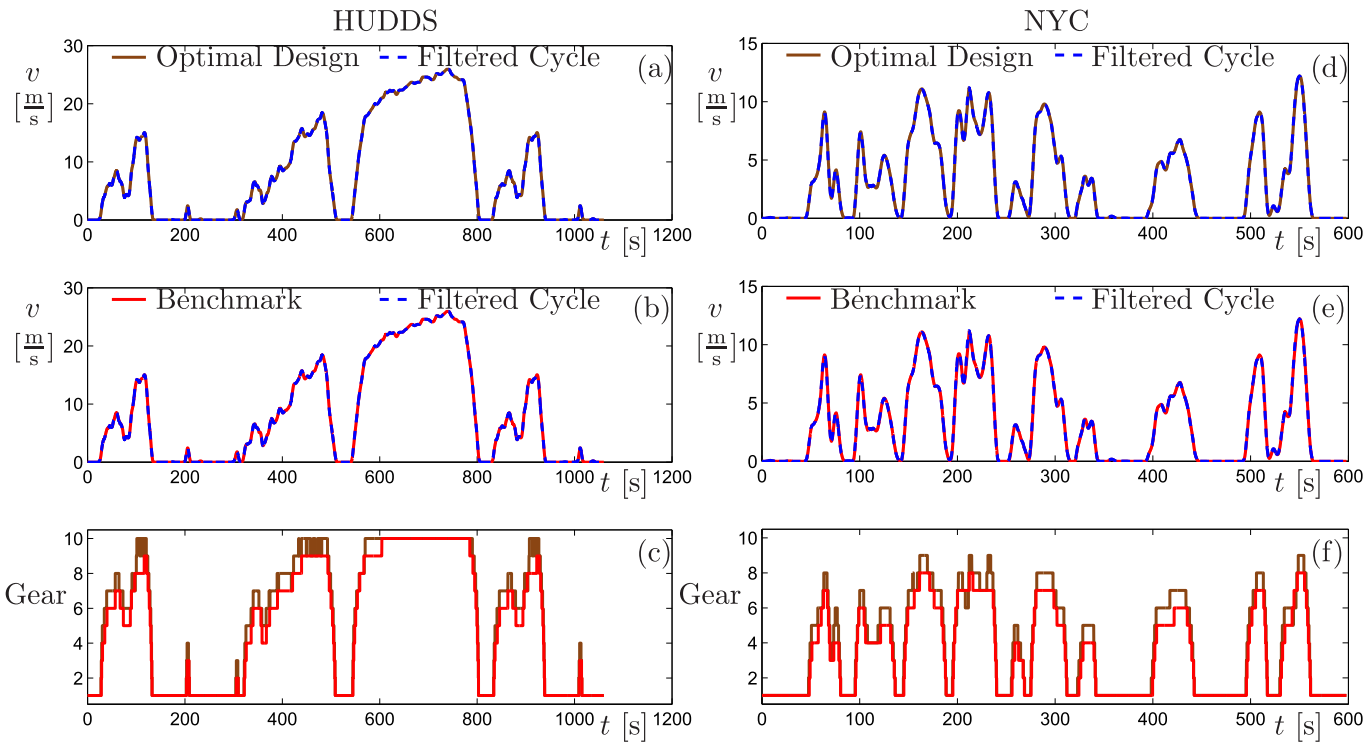

Fig. 10. Performance of the system (13) with the proposed gear shift schedule while following filtered cycles. The top (a) and (d) and middle (b) and (e) rows show the speed profiles of both optimal design (brown) and in-production benchmark design (red) while following the filtered cycles (dashed blue). The bottom (c) and (f) row shows gear profiles corresponding to the two difference speed profiles. (Best viewed in color.)

tries to follow a test cycle marked as a black dashed curve. The resulted time profile of the speed is shown by the solid brown curve in Fig. 8(b), while the time profile of the gear engaged is displayed in Fig. 8(c). In the last part of the cycle, the reference speed is set as a constant $v_{\mathrm{r}} = 15[\mathrm{m/s}]$, and the vehicle speed approaches this equilibrium. The corresponding trajectory is plotted in the (v, u)-plane in Fig. 8(a), with the gear engaged indicated by line type.

Next, we simulate cases where controller (6) is used to follow real driving cycles. In particular, we use two different EPA driving cycles, the heavy-duty urban dynamometer driving schedule (HUDDS) cycle and the New York City (NYC) cycle, shown as black dashed curves in Fig. 9(a), (b), (d), and (e), respectively. We compare the results using the proposed gear shift map and the in-production gear shift map implemented in the Navistar Prostar. The time evolution of the speed is shown in Fig. 9(a) and (d) for the optimal design (brown curves) and in Fig. 9(b) and (e) for the in-production benchmark design (red curves), while the corresponding gear profiles are shown in Fig. 9(c) and (f). The fuel performance and the tracking performance are summarized in Table I. In both cases, the controller manages to follow the reference speed closely, but the proposed gear shift map can achieve a better tracking performance with less fuel consumption.

However, frequent gear changes with the proposed optimal design can be seen, especially for the HUDDS cycle. For the HUDDS cycle, downshift at high speed happens when a large acceleration is needed, while for the NYC cycle, the frequent change is caused by both large deceleration and large acceleration.

TABLE I
FUEL CONSUMPTION AND TRACKING PERFORMANCE COMPARISON BETWEEN PROPOSED DESIGN AND IN-PRODUCTION BENCHMARK DESIGN WHILE FOLLOWING THE ORIGINAL DRIVING CYCLES

Optimal/Benchmark design	HUDDS	NYC
Fuel economy [MPG]	4.66/4.60	2.68/2.60
Maximum tracking error [m/s]	1.10/1.22	1.72/1.91
Average tracking error [m/s]	0.046/0.048	0.079/0.082

With traffic information available, an automated vehicle may plan the torque demand, so large variation of the torque demand can be avoided [23]. As an example, we filtered the original driving the HUDDS and the NYC cycles using a moving average filter of window size 5 [s], and fed the filtered cycle to the controller. This mimics a predictive controller for an automated vehicle with the prediction window of 2.5 [s]. The time profiles of the speed and the gear of the filtered cycles are shown in Fig. 10(a), (b), (d), and (e) as dashed blue curves. For filtered cycles, the controller still manages to follow the reference speed closely as shown by the brown and red curves. The corresponding gear profiles in Fig. 10(c) and (f) show that by providing a smoother speed profile (and therefore requiring lower torque), frequent gear changes can be avoided. In Table II, the fuel consumption and the tracking performance are summarized for the cases when the truck tries to follow the filtered cycle. It can be seen that a large improvement in fuel economy is achieved by filtering without creating a noticeable difference in the tracking error. The improvement of the proposed design over in-production design becomes more significant.

TABLE II
FUEL CONSUMPTION AND TRACKING PERFORMANCE COMPARISON BETWEEN PROPOSED DESIGN AND IN-PRODUCTION BENCHMARK DESIGN WHILE FOLLOWING THE FILTERED DRIVING CYCLES

Optimal/Benchmark design	HUDDS	NYC
Fuel economy [MPG]	5.44/5.23	3.17/3.00
Maximum tracking error compared to filtered cycle [m/s]	0.28/0.29	0.48/0.80
Average tracking error compared to filtered cycle [m/s]	0.027/0.027	0.052/0.054
Maximum tracking error compared to original cycle [m/s]	1.19/1.19	1.73/1.72
Average tracking error compared to original cycle [m/s]	0.122/0.122	0.196/0.198

These imply that by integrating the proposed gear shift design with proper speed profile planning, the automated vehicle could be driven both safely and fuel efficiently. To sum up, our framework guarantees the stability and efficiency of propulsion system, and enables further improvement in fuel economy with driving cycle planning for an automated vehicle while achieving better fuel performance.

VI. CONCLUSION AND FUTURE WORK

In this paper, we proposed a gear shift schedule design primarily intended for automated vehicles. We used Lyapunov arguments to prove the stability of equilibrium of the underlying constrained hybrid dynamical systems in the presence of constraints. Our design guarantees that the torque demand is delivered at the most fuel efficient gear. That is, fuel economy is improved without compromising drivability. It was shown that further improvements in fuel economy can be achieved by requesting smoother speed profile through automation.

In the future, we would like to: 1) extend the stability proof on hybrid system to cases with gear skip, power loss, and noninstantaneous gear shift; 2) improve the longitudinal controller by tuning of the PI-gains and using more sophisticated feedback design, such as feedback linearization; 3) explore other solutions at lower level to prevent frequent gear changes; and 4) investigate the effect of dynamic fuel consumption map on the proposed gear shift map.

APPENDIX

A. Proof of Lemma 3

We will prove the lemma in two steps. First, we show that without constraints, the equilibrium (9) is stable. Second, we show that adding (21), (22), and (24), the constrained working region (26) is still invariant, and the equilibrium (9) is still stable. Note that for a given v^*, equilibrium (9) is unique.

Defining the perturbations

$$\begin{aligned} \tilde{v} &= v - v^* \\ \tilde{u} &= u - u^* \end{aligned} \tag{28}$$

(8) can be rewritten as

$$\begin{aligned} \dot{\tilde{v}} &= -f(\tilde{v} + v^*) + \tilde{u} + u^* \\ \dot{\tilde{u}} &= -K_{\mathrm{P}}(-f(\tilde{v} + v^*) + \tilde{u} + u^*) - K_{\mathrm{I}}\tilde{v}. \end{aligned} \tag{29}$$

Choosing the Lyapunov function

$$V(\tilde{v}, \tilde{u}) = \frac{1}{2}K_{\mathrm{I}}\tilde{v}^2 + \frac{1}{2}(\tilde{u} + K_{\mathrm{P}}\tilde{v})^2 \tag{30}$$

with $K_{\mathrm{I}} > 0$ and $K_{\mathrm{P}} > 0$, we obtain the Lie derivative

$$\begin{aligned} \dot{V}(\tilde{v}, \tilde{u}) &= K_{\mathrm{I}}\tilde{v}\dot{\tilde{v}} + (\tilde{u} + K_{\mathrm{P}}\tilde{v})(\dot{\tilde{u}} + K_{\mathrm{P}}\dot{\tilde{v}}) \\ &= K_{\mathrm{I}}(-f(\tilde{v} + v^*) + f(v^*))\tilde{v} - K_{\mathrm{I}}K_{\mathrm{P}}\tilde{v}^2 \\ &= K_{\mathrm{I}}(-f'(\xi) - K_{\mathrm{P}})\tilde{v}^2. \end{aligned} \tag{31}$$

In the last step, the mean value theorem is applied to f assuming $v > 0$, which ensures that there exists ξ satisfying

$$f(\tilde{v} + v^*) - f(v^*) = f'(\xi)\tilde{v} \tag{32}$$

where $\xi = \xi(\tilde{v}) > 0$. Thus, (31) is negative semidefinite when $v > 0$. Applying the LaSalle–Krasovskii invariance principle, it can be shown that the largest invariant set within $\dot{V} = 0$ is $(\tilde{v}, \tilde{u}) = (0, 0)$. Therefore, the equilibrium is asymptotically stable.

Next, we show that in the presence of state constraints (24) and control constraints (21) and (22), the stability of the equilibrium can still be guaranteed. We show that the dynamics can be maintained along boundaries $v = 0$, $u = u_{\min}$, $u = u_{\max}$, and $m_{\mathrm{eff}}uv = P$, and that when a trajectory enters one of these boundaries (at time t_{en}) and leaves it (at time t_{ex}), then the Lyapunov function decreases between t_{in} and t_{ex}. We first determine the dynamics along the boundaries and determine the exit points $(v(t_{\mathrm{ex}}), u(t_{\mathrm{ex}}))$. Then, we show that the Lyapunov function (30) decreases while traveling along the boundary arcs, by comparing $v(t_{\mathrm{ex}}) - v^*$ with $v(t_{\mathrm{en}}) - v^*$, and $u(t_{\mathrm{ex}}) - u^*$ with $u(t_{\mathrm{en}}) - u^*$.

1) Along $v = 0$: Below the nullcline $u = f(v)$, we have $\dot{v} < 0$, while above it, we have $\dot{v} > 0$ (see Fig. 5). Corresponding to this, a trajectory can only enter the $v = 0$ boundary below the point where the nullcline intersects it (marked as a black plus in Fig. 5), i.e., $u(t_{\mathrm{en}}) < f(0) = \gamma\,\mathrm{g}$. Along this section, we have $\dot{v} = 0$ and $\dot{u} = K_{\mathrm{I}}v^* > 0$ according to the dynamics (8). That is, the trajectory keeps traveling upward on $v = 0$ until it reaches the nullcline at t_{ex} where $u(t_{\mathrm{ex}}) = f(0) = \gamma\,\mathrm{g}$. Comparing the states at t_{en} and t_{ex}, we have $v(t_{\mathrm{en}}) = v(t_{\mathrm{ex}}) = 0$ and $u(t_{\mathrm{en}}) < u(t_{\mathrm{ex}}) < u^*$, which imply

$$\begin{aligned} |v(t_{\mathrm{ex}}) - v^*| &= |v(t_{\mathrm{en}}) - v^*| \\ |u(t_{\mathrm{ex}}) - u^*| &< |u(t_{\mathrm{en}}) - u^*| \\ (u(t_{\mathrm{ex}}) - u^*)(v(t_{\mathrm{ex}}) - v^*) &< (v(t_{\mathrm{en}}) - v^*)(u(t_{\mathrm{en}}) - u^*). \end{aligned} \tag{33}$$

Substituting these into the Lyapunov function (30), we obtain

$$V(\tilde{v}(t_{\mathrm{ex}}), \tilde{u}(t_{\mathrm{ex}})) < V(\tilde{v}(t_{\mathrm{en}}), \tilde{u}(t_{\mathrm{en}})) \tag{34}$$

that is, the Lyapunov function decreases, while the trajectory travels along the $v = 0$ boundary.

2) Along $v = v_{\max}$: According to the definition (25), the $v = v_{\max}$ boundary is located below the $u = f(v)$ nullcline, yielding $\dot{v} < 0$. This means that no trajectory enters this boundary.

Before discussing the remaining three boundaries, we remark that according to the control constraints (21) and (22) and the monotonicity condition (10), we have

$$u_{\min} < f(v) < \min\left\{u_{\max}, \frac{P_{\max}}{v}\right\} \tag{35}$$

in the domain $0 < v < v_{\max}$ [see (24)].

3) Along $u = u_{\min}$: On the right-hand side of the nullcline $u = (K_I/K_P)(v^* - v) + f(v)$, we have $\dot{u} < 0$, while on the left-hand side of it, we have $\dot{u} > 0$. That is, a trajectory can enter the $u = u_{\min}$ boundary on the right-hand side of the nullcline. After traveling left along the boundary, it exits where the nullcline intersects the boundary (see black plus in Fig. 5). Consequently, we have $v(t_{ex}) < v(t_{en})$ and $u(t_{ex}) = u(t_{en}) = u_{\min}$.

However, in order to show that the Lyapunov function decreases while traveling along the boundary, additional arguments are needed. The normal unit vector to this boundary (pointing outbound) is given by $\mathbf{n}_{\min} = [0, -1]^T$. According to (8), when $u \equiv u_{\min}$, the vector field is given by $\mathbf{t}_{\min} = [-f(v) + u_{\min}, -K_P(-f(v) + u_{\min}) + K_I(v^* - v)]^T$. Then, staying on the boundary corresponds to

$$\mathbf{t}_{\min} \cdot \mathbf{n}_{\min} = K_P(-f(v) + u_{\min}) + K_I(v - v^*) > 0 \tag{36}$$

which holds on the right of the point where nullcline intersects the boundary, and it becomes zero at the intersection point. That is, using (35) and (36), we have $v(t_{ex}) > v^*$. Moreover, using $u \equiv u_{\min} \Rightarrow \tilde{u} < 0 \Rightarrow \dot{u} = \dot{\tilde{u}} = 0$, $\dot{v} = \dot{\tilde{v}} < 0$ and (10), (28), (35), and (36) in (31), we obtain the Lie derivative

$$\dot{V}(\tilde{v}, \tilde{u}) = \dot{v}\left(\left(K_I + K_P^2\right)\tilde{v} + K_P\tilde{u}\right). \tag{37}$$

Using the fact that $\dot{v} < 0, \tilde{v} > 0, K_P > 0$ and $\tilde{u} = -f(v^*) + u_{\min} > -f(v) + u_{\min}$, we have

$$\begin{aligned}\dot{V}(\tilde{v}, \tilde{u}) &< \dot{v}(K_I\tilde{v} + K_P(-f(v^*) + u_{\min})) \\ &< \dot{v}(K_I\tilde{v} + K_P(-f(v) + u_{\min})) \\ &= \dot{v}(\mathbf{t}_{\min} \cdot \mathbf{n}_{\min}) < 0.\end{aligned} \tag{38}$$

That is, the Lyapunov function decreases along the $u = u_{\min}$ boundary.

Note that it is possible that the nullcline intersects the $u = u_{\min}$ boundary at $v > v_{\max}$. In such a case, no trajectory enters the boundary $u = u_{\min}$.

4) Along $u = u_{\max}$: This boundary can be handled similar to the $u = u_{\min}$ boundary. A trajectory may enter the boundary on the left-hand side of the nullcline, and after traveling right, it exits where the nullcline intersects the boundary (see black plus in Fig. 5). Consequently, we have $v(t_{ex}) > v(t_{en})$ and $u(t_{ex}) = u(t_{en}) = u_{\max}$.

Similar to the $u = u_{\min}$ boundary, it can be shown that the Lyapunov function decreases when the trajectory travels along the boundary. The normal unit vector to this boundary (pointing outbound) is given by $\mathbf{n}_{\max} = [0, 1]^T$. According to (8), along the $u = u_{\max}$ boundary, the vector field is given by $\mathbf{t}_{\max} = [-f(v) + u_{\max}, -K_P(-f(v) + u_{\max}) + K_I(v^* - v)]^T$, yielding

$$\mathbf{t}_{\max} \cdot \mathbf{n}_{\max} = -K_P(-f(v) + u_{\max}) - K_I(v - v^*) > 0. \tag{39}$$

This holds only on the left of the point where nullcline intersects the boundary, and it becomes zero at the intersection point. That is, using (35) and (39), we have $v^* > v(t_{ex}) > v(t_{en})$ and $u(t_{ex}) = u(t_{en}) = u_{\max}$. When traveling along the boundary, the Lie derivative is the same as (38) and again using (10), (28), (35), and (39), one can show that it is negative, i.e., the Lyapunov function decreases along the $u = u_{\min}$ boundary.

Note that it is possible that the nullcline intersects the $u = u_{\max}$ boundary at $v > v_{\text{switch}}$ [see (23)] or $v < 0$. In the former case, the no trajectory enters the $u = u_{\max}$ boundary. The latter case implies that no trajectory exits within $[0, v_{\text{switch}}]$, but continues to travel along the boundary $m_{\text{eff}}uv = P_{\max}$, which will be handled in the following.

5) Along $m_{\text{eff}}uv = P_{\max}$: This boundary can only be entered when $v \geq v_{\text{switch}}$ [see (23)], and we have $\dot{v} > 0$, since this boundary is above the nullcline $u = f(v)$. We denote $\bar{P} = (P_{\max}/m_{\text{eff}})$ in the rest of proof for compact description. Note that this boundary is neither horizontal nor vertical. Consequently, one cannot use the nullcline to determine where this trajectory exits the boundary. The normal vector to this boundary pointing outbound is given by $\mathbf{n}_P = [(\bar{P}/v^2), 1]^T$, while vector field is given by $\mathbf{t}_P = [-f(v) + \bar{P}/v, -K_P(-f(v) + \bar{P}/v) + K_I(v^* - v)]^T$ [see (8)]. In order to stay along the boundary, we need

$$(\mathbf{t}_P \cdot \mathbf{n}_P)(v) = \left(\frac{\bar{P}}{v^2} - K_P\right)\left(-f(v) + \frac{\bar{P}}{v}\right) - K_I(v - v^*) > 0. \tag{40}$$

This requires that $v_{\text{switch}} < v < v^*$, and otherwise, due to (27) and (35), both terms in (40) are negative. Indeed, to enter the boundary, we need $(\mathbf{t}_P \cdot \mathbf{n}_P)(v(t_{en})) > 0$, while at the exit point, $(\mathbf{t}_P \cdot \mathbf{n}_P)(v(t_{ex})) = 0$.

In fact, if K_P and K_I satisfy (27), there exists $\bar{v} \in (0, v_{\text{switch}})$ such that $K_P\bar{v}^2 - \bar{P} = 0$, so $(\mathbf{t}_P \cdot \mathbf{n}_P)(\bar{v}) = K_I(v^* - \bar{v}) > 0$. On the other hand, due to (27) and (35), $(\mathbf{t}_P \cdot \mathbf{n}_P)(v) < 0$ for all $v \geq v^*$. Thus, there exists $v \in (\bar{v}, v^*)$, such that $(\mathbf{t}_P \cdot \mathbf{n}_P)(v) = 0$ (see the black plus on the curve $uv = \bar{P}$ in Fig. 5). Recall that v is increasing along the boundary. Using (10) and (35), we have $v(t_{en}) < v(t_{ex}) < v^*$. Using (10) and (28) in (31), the Lie derivative becomes

$$\dot{V}(\tilde{v}, \tilde{u}) = K_I\tilde{v}(-f(v) + u^*) - K_PK_I\tilde{v}^2 < -K_PK_I\tilde{v}^2 < 0. \tag{41}$$

That is, the Lyapunov function decreases along the $uv = \bar{P}$ boundary.

Note that $(\mathbf{t}_P \cdot \mathbf{n}_P)(v(t_{ex})) = 0$ may occur for $v(t_{ex}) < v_{\text{switch}}$. In this case, the trajectory does not enter the $uv = \bar{P}$ boundary.

Therefore, we can conclude that if we choose K_P, K_I according to (27), when traveling along boundary arcs, the value of the Lyapunov function decreases. This, together with that the Lyapunov function decreases along the trajectories in the interior, the equilibrium (9) is asymptotically stable.

B. Proof of Theorem 1

Recall (28) and let us denote working region of engine in $(\tilde{v}, \tilde{u})$-space as $\mathscr{X}$ [see (26)]. Using Lemma 2 and

TABLE III
DATA OF A 2012 NAVISTAR PROSTAR TRUCK [24]

Parameter	Value
Mass (m)	29484 [kg]
Air Drag Coefficient (k)	3.84 [kg/m]
Tire Rolling Radius (R)	0.504 [m]
Tire Rolling Resistance Coefficient (γ)	0.006
Maximum Acceleration ($u_{\max}$)	2 [m/s^2]
Rotational Element Inertia (J)	39.9 [kg·m^2]
Gravitational Constant (g)	9.81 [m/s^2]
Number of Forward Gears	10
1st Gear Ratio/Efficiency	12.94/0.97
2nd Gear Ratio/Efficiency	9.29/0.97
3rd Gear Ratio/Efficiency	6.75/0.97
4th Gear Ratio/Efficiency	4.9/0.97
5th Gear Ratio/Efficiency	3.62/0.97
6th Gear Ratio/Efficiency	2.64/0.97
7nd Gear Ratio/Efficiency	1.90/0.97
8rd Gear Ratio/Efficiency	1.38/0.98
9th Gear Ratio/Efficiency	1/0.99
10th Gear Ratio/Efficiency	0.74/0.98
Final Drive Ratio /Efficiency	3.73/0.96

Assumption 1, a two-neighbor ε-partition is generated by gear change as $\bigcup_{i=1}^{N} P^{\mathrm{N}\varepsilon}$ over $(\tilde{v}, \tilde{u})$-space. We define $Q_{i,j}^{\mathrm{N}\varepsilon} = P_i^{\mathrm{N}\varepsilon} \bigcap P_j^{\mathrm{N}\varepsilon}$. The initial states are $(\tilde{v}_0, \tilde{u}_0)$ at $t = 0$. According to Lemma 3, the trivial equilibrium of (29) is asymptotically stable. Define the domain $D_\delta = \{(\tilde{v}, \tilde{u}) | V(\tilde{v}, \tilde{u}) \leq \delta\} \bigcap \mathscr{X}$, where V is the Lyapunov function (30). In the following, we use the abbreviated notation $D_{V(\tilde{v}_0,\tilde{u}_0)}$, by which we mean D_δ with $\delta = V(\tilde{v}_0, \tilde{u}_0)$. Without loss of generality, we assume that the equilibrium (v^*, u^*) is located in $P_i^{\mathrm{N}\varepsilon}$, while the initial state $(\tilde{v}_0, \tilde{u}_0)$ can be in any gear. Then, there are three possibilities. The trajectories of all the possibilities are shown in Fig. 6 by brown curves with gear engaged implied by line styles, where initial conditions are denoted by brown crosses, while equilibrium is denoted by black dots.

1) The equilibrium is located in a nonoverlap region (i.e., $(v^*, a_d^*) \notin Q_{i,j}^{\mathrm{N}\varepsilon} \forall j \neq i$), and the initial state $(\tilde{v}_0, \tilde{u}_0) \in D_{V(\tilde{v}_0,\tilde{u}_0)} \subseteq P_i^{\mathrm{N}\varepsilon}$. If $(\tilde{v}_0, \tilde{u}_0) \in P_i^{\mathrm{N}\varepsilon} \bigcap P_j^{\mathrm{N}\varepsilon}$ where $j \in N_i$, and the system starts in the jth gear, then one gear change will happen and the trajectory settles to the ith gear, yielding a stable equilibrium. If, instead, the system starts in the ith gear, then no gear change will happen, while the trajectory approaches the equilibrium. The corresponding trajectory is shown in Fig. 6, denoted by case 1.
2) The equilibrium is located in a nonoverlap region, but the trajectory travels through different regions, that is $D_{V(\tilde{v}_0,\tilde{u}_0)} \bigcap P_j^{\mathrm{N}\varepsilon} \backslash Q_{i,j}^{\mathrm{N}\varepsilon} \neq \emptyset, \exists j \neq i$. In this case, multiple gear shifts may occur. By Assumption 1, there is a nonzero dwell time between two consecutive gear shifts. Then, $\exists T > 0$ such that $\forall t > T$, $D_{V(\tilde{v}(t),\tilde{u}(t))} \subseteq P_i^{\mathrm{N}\varepsilon}$. Since T is finite, it will enter and leave $P_j^{\mathrm{N}\varepsilon}, \forall j \neq i$ only finite times. The corresponding trajectories are shown in Fig. 6, denoted by case 2. Therefore, the gear will still settle down to the ith gear, and the equilibrium will be stable.
3) The equilibrium is located in an overlap region, i.e., $\exists j \in N_i$, such that $(v^*, u^*) \in Q_{i,j}^{\mathrm{N}\varepsilon}$. If $D_{V(\tilde{v}_0,\tilde{u}_0)} \subset Q_{i,j}^{\mathrm{N}\varepsilon}$, the states converge to the equilibrium without changing gears and the equilibrium is stable. The final gear will be the same as the initial gear, and thus could be either ith or jth. If $D_{V(\tilde{v}_0,\tilde{u}_0)} \not\subset Q_{i,j}^{\mathrm{N}\varepsilon}$, then $\exists T > 0$ such that $\forall t > T$, $D_{V(\tilde{v}(t),\tilde{u}(t))} \subseteq Q_{i,j}^{\mathrm{N}\varepsilon}$. Since T is finite, the trajectory will enter and leave $P_j^{\mathrm{N}\varepsilon}, (j \neq i)$ only finite times. Therefore, the gear will still settle down at the same gear as $(\tilde{v}(T), \tilde{u}(T))$ (also could be either i or j). The corresponding trajectories are shown in Fig. 6, denoted by case 3.

C. Table of Parameter of a Navistar Truck

See Table III.

ACKNOWLEDGMENT

The authors would like to thank the NAVISTAR company for providing the source data used in this paper.

REFERENCES

[1] H. Peng, "Connected and automated vehicles: The roles of dynamics and control," *Mech. Eng.*, vol. 138, no. 12, pp. S4–S11, 2016.
[2] G. Orosz, "Connected cruise control: Modelling, delay effects, and nonlinear behaviour," *Vehicle Syst. Dyn.*, vol. 54, no. 8, pp. 1147–1176, 2016.
[3] J. I. Ge and G. Orosz, "Dynamics of connected vehicle systems with delayed acceleration feedback," *Transp. Res. C, Emerg. Technol.*, vol. 46, pp. 46–64, Sep. 2014.
[4] L. Zhang and G. Orosz, "Motif-based design for connected vehicle systems in presence of heterogeneous connectivity structures and time delays," *IEEE Trans. Intell. Transp. Syst.*, vol. 17, no. 6, pp. 1638–1651, Jun. 2016.
[5] S. Bai, J. M. Maguire, and H. Peng, *Dynamic Analysis and Control System Design of Automatic Transmissions*. Warrendale, PA, USA: SAE International, 2013.
[6] D. Kim, H. Peng, S. Bai, and J. M. Maguire, "Control of integrated powertrain with electronic throttle and automatic transmission," *IEEE Trans. Control Syst. Technol.*, vol. 15, no. 3, pp. 474–482, May 2007.
[7] V. D. Ngo, J. A. C. Navarrete, T. Hofman, M. Steinbuch, and A. Serrarens, "Optimal gear shift strategies for fuel economy and driveability," *Proc. Inst. Mech. Eng. D, J. Automobile Eng.*, vol. 277, no. 10, pp. 1398–1413, 2013.
[8] A. Fofana *et al.*, "Multi-objective genetic algorithm for an automatic transmission gear shift map," *IFAC-PapersOnLine*, vol. 49, no. 3, pp. 123–128, 2016.
[9] G. Qin, A. Ge, and J.-J. Lee, "Knowledge-based gear-position decision," *IEEE Trans. Intell. Transp. Syst.*, vol. 5, no. 2, pp. 121–125, Jun. 2004.
[10] J. Tan, X. Yin, Y. Lei, and A. Ge, "Research on a neural network model based automatic shift schedule with dynamic 3-parameters," SAE Tech. Paper 2005-01-1597, Apr. 2005.
[11] G. Li and J. Hu, "Modeling and analysis of shift schedule for automatic transmission vehicle based on fuzzy neural network," in *Proc. IEEE 8th World Congr. Intell. Control Autom. (WCICA)*, Jul. 2010, pp. 4839–4844.
[12] Y. G. Liu, D. T. Qin, Z. Z. Lei, and R. Ding, "Intelligent correction of shift schedule for dual clutch transmissions based on different driving conditions," *Appl. Mech. Mater.*, vols. 121–126, pp. 3982–3987, Oct. 2011.
[13] H. Lin and P. J. Antsaklis, "Stability and stabilizability of switched linear systems: A survey of recent results," *IEEE Trans. Autom. Control*, vol. 54, no. 2, pp. 308–322, Feb. 2009.
[14] M. S. Branicky, "Multiple Lyapunov functions and other analysis tools for switched and hybrid systems," *IEEE Trans. Autom. Control*, vol. 43, no. 4, pp. 475–482, Apr. 1998.
[15] M. Bernardo, C. Budd, A. R. Champneys, and P. Kowalczyk, *Piecewise-smooth Dynamical Systems: Theory and Applications* (Applied Mathematical Sciences), vol. 163. London, U.K.: Springer, 2008.

[16] J. Liu, X. Liu, and W.-C. Xie, "On the (h_0, h)-stabilization of switched nonlinear systems via state-dependent switching rule," *Appl. Math. Comput.*, vol. 217, no. 5, pp. 2067–2083, 2010.
[17] Y. Jin, J. Fu, Y. Zhang, and Y. Jing, "Reliable control of a class of switched cascade nonlinear systems with its application to flight control," *Nonlinear Anal., Hybrid Syst.*, vol. 11, pp. 11–21, Jan. 2014.
[18] J. Liu, N. Ozay, U. Topcu, and R. M. Murray, "Synthesis of reactive switching protocols from temporal logic specifications," *IEEE Trans. Autom. Control*, vol. 58, no. 7, pp. 1771–1785, Jul. 2013.
[19] A. Alam, "Fuel-efficient heavy duty vehicle platooning," Ph.D. dissertation, Dept. Elect. Eng., KTH Roy. Inst. Technol., Stockholm, Sweden, 2014.
[20] J. B. Heywood, *Internal Combustion Engine Fundamentals*. New York, NY, USA: McGraw-Hill, 2002.
[21] K. J. Aström and R. M. Murray, *Feedback Systems—An Introduction for Scientists and Engineers*. Princeton, NJ, USA: Princeton Univ. Press, 2010.
[22] L. Zhang, J. Sun, and G. Orosz, "Hierarchical design of connected cruise control in the presence of information delays and uncertain vehicle dynamics," *IEEE Trans. Control Syst. Technol.*, 2017, doi: 10.1109/TCST.2017.2664721.
[23] C. R. He, H. Maurer, and G. Orosz, "Fuel consumption optimization of heavy-duty vehicles with grade, wind, and traffic information," *J. Comput. Nonlinear Dyn.*, vol. 11, no. 6, p. 061011, 2016.
[24] "Maxxforce 11 and 13 liter engines," Navistar Inc., Lisle, IL, USA, Tech. Rep. TMT-121107, 2011.

Chaozhe R. He received the B.Sc. degree in applied mathematics from the Beijing University of Aeronautics and Astronautics, Beijing, China, in 2012. He is currently pursuing the Ph.D. degree in mechanical engineering with the University of Michigan, Ann Arbor, MI, USA.

His current research interests include dynamics and control of connected vehicles, optimal control theory, and its applications.

Wubing B. Qin received the B.Eng. degree from the Huazhong University of Science and Technology, Wuhan, China, in 2011. He is currently pursuing the Ph.D. degree in mechanical engineering with the University of Michigan, Ann Arbor, MI, USA.

His current research interests include dynamics and control of connected vehicles and nonlinear and stochastic systems with time delays.

Necmiye Ozay received the B.S. degree from Boğaziçi University, Istanbul, Turkey, in 2004, the M.S. degree from Pennsylvania State University, University Park, PA, USA, in 2006, and the Ph.D. degree from Northeastern University, Boston, MA, USA, in 2010, all in electrical engineering.

She was a Post-Doctoral Scholar with the California Institute of Technology, Pasadena, CA, USA, from 2010 to 2013. She is currently an Assistant Professor of electrical engineering and computer science with the University of Michigan, Ann Arbor, MI, USA. Her current research interests include dynamical systems, control, optimization, formal methods with applications in cyberphysical systems, system identification, verification and validation, and autonomy.

Dr Ozay was the recipient of the DARPA Young Faculty Award in 2014, the NSF CAREER Award, the NASA Early Career Faculty Award, and the DARPA Directors Fellowship in 2016.

Gábor Orosz received the M.Sc. degree in engineering physics from the Budapest University of Technology, Budapest, Hungary, in 2002, and the Ph.D. degree in engineering mathematics from the University of Bristol, Bristol, U.K., in 2006.

He held the post-doctoral positions with the University of Exeter, Exeter, U.K., and the University of California, Santa Barbara, CA, USA, before joining the University of Michigan, Ann Arbor, MI, USA, in 2010, where he is currently an Associate Professor of mechanical engineering. His current research interests include nonlinear dynamics and control, time-delay systems, networks, and complex systems with applications on connected and automated vehicles and biological networks.